



# Slide-free virtual histochemistry (Part I): development via nonlinear optics

SIXIAN YOU,<sup>1,2</sup> YI SUN,<sup>1</sup> ERIC J. CHANEY,<sup>1</sup> YOUNG ZHAO,<sup>1</sup>  
JIANXIN CHEN,<sup>3,5</sup> STEPHEN A. BOPPART,<sup>1,2,4,6</sup> AND HAOHUA TU<sup>1,7</sup>

<sup>1</sup>Beckman Institute for Advanced Science and Technology, University of Illinois at Urbana-Champaign, Urbana, IL 61801, USA

<sup>2</sup>Department of Bioengineering, University of Illinois at Urbana-Champaign, Urbana, IL 61801, USA

<sup>3</sup>Fujian Provincial Key Laboratory for Photonics Technology, Key Laboratory of OptoElectronic Science and Technology for Medicine of Ministry of Education, Fujian Normal University, Fuzhou, 350007, China

<sup>4</sup>Department of Electrical and Computer Engineering, Carle-Illinois College of Medicine, University of Illinois at Urbana-Champaign, Urbana, IL 61801, USA

<sup>5</sup>chenjianxin@fjnu.edu.cn

<sup>6</sup>boppart@illinois.edu

<sup>7</sup>htu@illinois.edu

**Abstract:** Histochemistry is a microscopy-based technology widely used to visualize the molecular distribution in biological tissue. Recent developments in label-free optical imaging has demonstrated the potential to replace the conventional histochemical labels/markers (fluorescent antibodies, organic dyes, nucleic acid probes, and other contrast agents) with diverse optical interactions to generate histochemical contrasts, allowing “virtual” histochemistry in three spatial dimensions without preparing a microscope slide (i.e. labor-intensive sample preparation). However, the histochemical information in a label-free optical image has often been rather limited due to the difficulty in simultaneously generating multiple histochemical contrasts with strict spatial co-registration. Here, in the first part (Part I) of this two-part series study, we develop a technique of slide-free virtual histochemistry based on label-free multimodal multiphoton microscopy, and simultaneously generate up to four histochemical contrasts from *in vivo* animal and *ex vivo* human tissue. To enable this functionality, we construct and demonstrate a robust fiber-based laser source for clinical translation and phenotype a wide variety of vital cells in unperturbed mammary tissue.

© 2018 Optical Society of America under the terms of the [OSA Open Access Publishing Agreement](#)

## 1. Introduction

A long-sought goal in biomedical engineering is to perform tissue molecular imaging in a clinical setting, in real-time, *in vivo*, without stains, without slides, and in three-dimensions at optical resolutions. To this purpose, histochemical imaging contrasts have been generated from fresh unlabeled tissue specimens by varying the incident light that interacts with the specimen, rather than by treating (e.g., histologically processing and labeling) the specimen and illuminating it with fixed light. Versatile approaches of this type of imaging include tuning the optical frequency difference in stimulated Raman scattering microscopy (SRS) to obtain molecular vibration contrasts [1], varying the absorption wavelength in photoacoustic microscopy to obtain absorption contrasts [2], and programming light excitation and detection in multimodal multiphoton microscopy to obtain diverse nonlinear optical contrasts [3]. However, for fast *in vivo* imaging, only one contrast (black-and-white image) is generated in one raster scan of the specimen, typically. It is possible to obtain additional types of contrast by scanning the same tissue section with different conditions of light excitation and/or detection, but this rescanning does not guarantee the co-localization of the two contrasts in *in vivo* imaging and increases the risk of sample photo-damage. Temporal multiplexing of

different excitation conditions at each imaging pixel has been implemented for both SRS [4] and photoacoustic microscopy (e.g. in oxygen-metabolic vasculature imaging [5]) to simultaneously acquire two spectroscopic contrasts in one scan. This methodology guarantees co-localization of image data, but for imaging at a given signal-to-noise ratio, retains the risk of sample photo-damage.

With no such risk, spectral multiplexing of different detection channels has been realized in simultaneous multimodal multiphoton imaging of plant cells at 1230-nm excitation [6]. We envision that this technique should allow multicolor “virtual” histochemistry of animal/human tissue at 1110-nm excitation via two-photon excited auto-fluorescence (2PAF, yellow), three-photon excited auto-fluorescence (3PAF, cyan), second-harmonic generation (SHG, green), and third-harmonic generation (THG, magenta) (Fig. 1(a)). The shift of the excitation wavelength from 1230-nm to 1110-nm allows for spectrally-separated detection of the four colored contrasts, in which the 3PAF and 2PAF contrasts correspond, respectively, to the emission bands of NADH and FAD with minimum spectral overlap (Fig. 1(b), upper panel) [7–9]. A recent study demonstrated the power of simultaneous label-free autofluorescence-multiharmonic (SLAM) microscopy for intravital imaging based on a solid-state laser-induced fiber supercontinuum [8]. To further the clinical applicability of this methodology, this paper leverages the recent advances in the fiber-laser industry by building the SLAM imaging platform on a fiber-laser-induced supercontinuum for better stability and ease of operation. Further, the applicability of this new imaging platform is evaluated with a broad array of biological specimens.

This paper forms the first part (Part I) of our two-part series study on the envisioned label-free multiphoton histochemical imaging, with a focus on the technological development of slide-free virtual histochemistry via nonlinear optics in both free-space and fiber configuration. The second part (Part II) [10] of this two-part series study will focus on the application and unique capability of the developed slide-free virtual histochemistry to detect field cancerization in peri-tumoral fields.

## 2. Laser and microscope

The desired excitation band centered at 1110-nm is not directly available from femtosecond fiber lasers with limited wavelength tunability [11]. We therefore sought to replace the solid-state laser with a femtosecond fiber laser as the master laser for coherent fiber supercontinuum generation [12,13], which has been employed in multiphoton imaging of human skin [14] (Table 1). All these prior studies chose to custom build the master fiber laser. It is unclear whether this choice is due to the noise or decoherence mechanism [15] that might be associated with widely available commercial femtosecond fiber lasers. Taking the hint from the master fiber laser that was custom built to generate near transform-limited pulses [12,13], we selected a commercial laser that produced a small time-bandwidth product (Table 1).

This industrial fiber laser (Satsuma, Amplitude Systemes) is widely used in laser-assisted *in situ* keratomileusis (LASIK) eye surgery [16], but has not been actively pursued for biomedical imaging. The free-space coupling of 2.3 W laser power to the fiber generated a supercontinuum output of 1.8 W (Fig. 1(c)). The multiphoton microscope in this study largely followed the setup reported in a prior study [8]. The band of  $1110 \pm 30$  nm in the supercontinuum was spectrally selected by a pulse shaper (MIIPS Box640, Biophotonics Solutions) with an average output power of 50 mW. Then the near-transform-limited pulses  $\sim 35$  fs (FWHM) were raster scanned by a galvanometer mirror pair (6215H, Cambridge Technology) (Fig. 1(a), upper panel).

An objective with high UV transmission (UAPON 40XW340, N.A. 1.15, Olympus) was used to produce a field-of-view of  $350 \times 350 \mu\text{m}^2$ . The loss along the excitation beam path resulted in an average focusing power of  $\sim 20$  mW on the tissue (well below the ANSI standard of  $\sim 100$  mW at this wavelength). The reflected 4-channel multiphoton signals were then spectrally separated by appropriate dichroic mirrors and optical filters (Semrock, Inc.)

(Fig. 1(a), upper panel) and simultaneously collected by 4 photomultipliers (H7421-40, Hamamatsu). By directly comparing the pulse-shaped fiber supercontinuum generated from this fiber laser with that from a similar solid-state laser (femtoTrain, Spectra-Physics Inc.) (Table 1) (Fig. 1(c)), we obtained comparable imaging performance from the same sample. The additional noise or decoherence associated with the fiber laser-induced supercontinuum, if present, has no appreciable effect on our tetra-modal imaging. Also, the feasibility to simultaneously image NADH and FAD by 1110-nm excitation via the 3PAF and 2PAF detection channels was demonstrated by imaging the NADH and FAD solutions (Fig. 1(b), lower panel).

There are several practical benefits associated with this replacement of the master laser. First, the bulky, water cooled, and frequently unstable solid-state laser is replaced with a compact air-cooled robust fiber laser suitable for portable applications [1]. Second, the deterministic supercontinuum generation in the normal dispersion regime of the photonic crystal fiber, and subsequent pulse shaping, are both passive optical processes (in comparison to the active processes of lasing) stable against mechanical and thermal disturbance [15]. This stability, along with the excellent beam pointing stability of the fiber laser, enables long-term stable operation (hundreds of hours over 6 months) of the supercontinuum source free of realignment or service. Third, daily operation of the supercontinuum source resembles its turn-key master fiber laser, allowing a user with minimum laser training to begin imaging after only a 5-min warmup.

**Table 1. Some coherent fiber supercontinuum sources for general multiphoton microscopy.**

Reference in text	3	14	This study	
Tunable $\lambda$ (nm)	770-1280	1030-1215	900-1180	900-1180
Pulse width $\tau$ (fs)	~25	50	~25	~25
Average power (mW)	10-30	~500	10-100	10-100
Repetition rate $f$ (MHz)	80	55	10	10
Peak-power factor $(f\tau)^{-1}$	$5.0 \times 10^5$	$3.6 \times 10^5$	$4.0 \times 10^6$	$4.0 \times 10^6$
Master laser	Solid-state Yb:KGW laser	Custom Yb:fiber laser	Solid-state Yb:KGW laser	Commercial Yb:fiber laser
Nonlinear fiber core size ( $\mu\text{m}$ )	2.3	8	15	15
Dispersion compensation module	Programmable pulse shaper	Grating compressor	Programmable pulse shaper	Programmable pulse shaper
Access to wavelengths	simultaneous	sequential	simultaneous	simultaneous

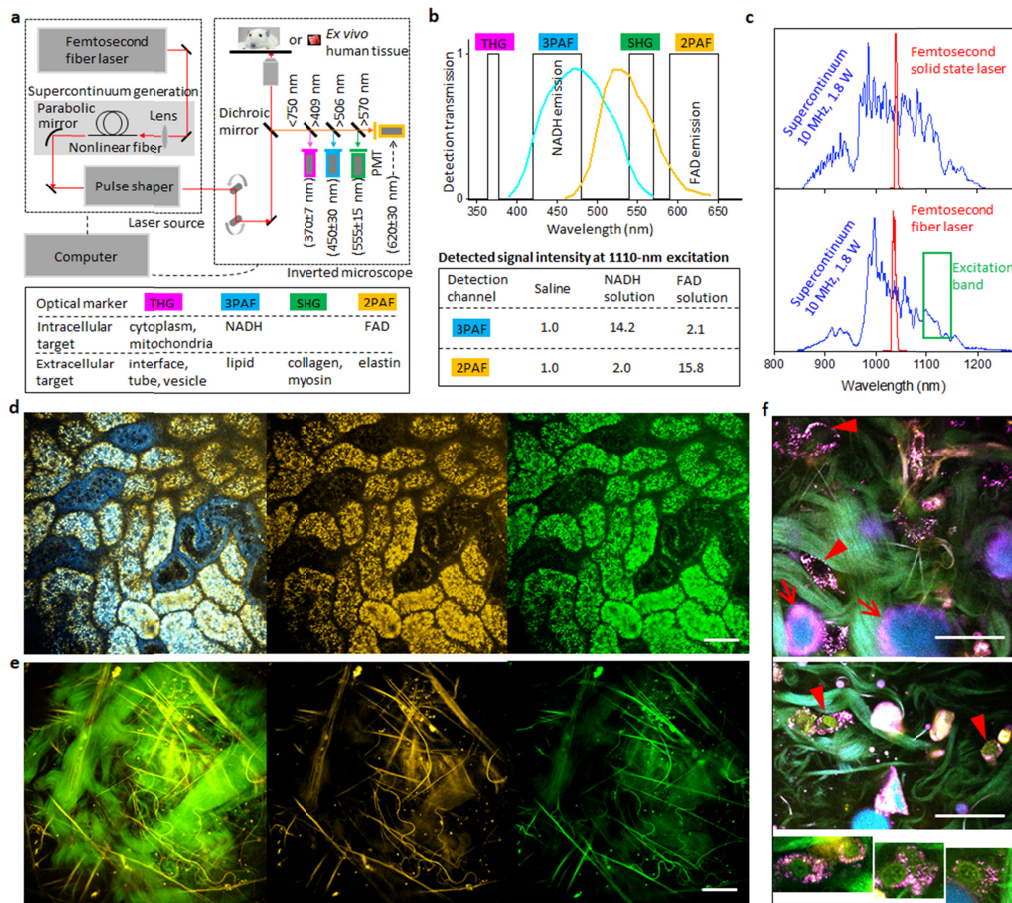


Fig. 1. Slide-free virtual histochemistry of fresh untreated tissue using a fiber laser-induced supercontinuum source. (a) Schematic of tetra-modal inverted microscope, with specific sets of dichroic mirrors, optical filters, photomultipliers (PMTs) (upper panel) that dictate 4 optical markers/colors (lower panel). (b) Upper panel: transmission bands of detection channels against emission spectra of NADH and FAD; lower panel: signal generation from an FAD solution, an NADH solution, and saline (control), with intensity computed by averaging the pixel values of the image in corresponding channels. (c) Comparison of supercontinuum source generated by a solid-state laser (upper panel) and the fiber laser in this study (lower panel). (d) Images of epithelial cells in a mouse kidney showing combined 2PAF-3PAF contrasts of the tetra-modal imaging (left panel), 2PAF contrast alone (middle panel), and 2PAF contrast at reprogrammed (920-nm) excitation detected by the SHG channel of the tetra-modal imaging. (e) Images of collagen and elastin fibers in human breast tissue showing combined 2PAF-3PAF contrasts of the tetra-modal imaging (left panel), 2PAF contrast alone (middle panel), and 2PAF contrast at reprogrammed (920-nm) excitation detected by the SHG channel of the tetra-modal imaging. (f) Tetra-modal images of human breast tissue showing cyan-colored lipid vacuoles of adipocytes (arrows) and magenta-colored cytoplasm/mitochondria of certain cells (arrowheads) before acridine orange labeling (upper panel) and after the labeling (lower panels). An average focusing power of  $\sim 20$  mW was used on the tissue. Scale bars: 50  $\mu\text{m}$ .

### 3. Materials

#### 3.1 Human and rat tissue specimens

Female rats (F344, Harlan) were used in this study under a protocol approved by the Institutional Animal Care and Use Committee at the University of Illinois Urbana-Champaign. For the experimental group, mammary tumors were induced in 7-week old rats by intraperitoneally injecting N-nitroso-N-methylurea (NMU, Sigma) at a concentration

of 55 mg/kg. The first injection was performed on the left abdominal side, and a second injection was performed one week later on the right abdominal side. The lesions were first palpable from the abdominal surface about 4 weeks after the second injection, and were allowed to grow up to 1.5 cm afterward. For the control group, an equal amount of saline was injected at each time point to account for plausible effects from the injection. Small surgeries were performed to expose the mammary glands of the rats from both groups 6-16 weeks after the second injection. The rats underwent *in vivo* imaging of the mammary tissue and were then euthanized.

Human breast cancer tissue (from tumor resection surgery) and normal tissue (from breast reduction surgery) were obtained under a protocol approved by the Institutional Review Boards at the University of Illinois at Urbana-Champaign and Carle Foundation Hospital. The permission for investigational use of all tissue specimens was obtained from subjects who preoperatively signed an informed consent. The tissue specimens were stored in saline-filled conical tubes and transported on ice for imaging within 12 hours after surgery.

### 3.2 *In vivo* animal imaging

An experimental rat with palpable lesion(s) or a control rat was anesthetized with isoflurane, and a small incision was made in the abdominal skin to expose a tumor (~1 cm) or normal mammary gland. The surrounding skin was flipped on a microscope coverslip so that the field-of-view could be arbitrarily placed at the visually detected lesion site. The rat itself was positioned on a three-dimensional motorized piezoelectric stage to allow depth-resolved imaging and large-field imaging with a mosaic of high-resolution fields-of-view. The imaging focal plane was placed 5-100  $\mu\text{m}$  below the sample surface. Anesthesia was maintained throughout the imaging session while the rat was kept warm at physiologic temperature with a heating pad and blanket. The galvanometer mirror-based scanning along with the unique optical excitation allowed acquisition of multi-contrast multiphoton images ( $512 \times 512$  pixelated frame with  $350 \times 350 \mu\text{m}^2$  standard field-of-view) at a frame rate of 0.5 Hz, corresponding to a pixel dwell time of ~8  $\mu\text{s}$ . The full “field-of-view” image presented in the figures were a result of mosaic acquisition (3x3, or 5x5 depending on the final image size). Raw data from the photomultipliers were used to produce all images without additional processing such as deconvolution or maximum intensity projection. This *in vivo* imaging of rat mammary tissue was also employed in *ex vivo* imaging of human breast tissue without the *in vivo* aspects.

## 4. Results

### 4.1 Characterizing slide-free virtual histochemistry

To demonstrate that our fiber laser-based source retained the capability of the programmable light multiphoton imaging [3], we first performed the tetra-modal imaging on *ex vivo* mouse kidney and readily differentiated the NADH-rich (cyan-colored) epithelial cells from FAD-rich (yellow-colored) epithelial cells in kidney tubules and collecting ducts (Fig. 1(d), left two panels) [17]. We then reprogrammed the excitation to generate 30-fs 920-nm pulses [3], and conducted FAD imaging through the SHG detection channel of the tetra-modal imaging, according to the established excitation/detection wavelengths of this endogenous compound [7]. As expected, only the FAD-rich epithelial cells were observed after the reprogramming (Fig. 1(d), right panel). Similarly, we first performed the tetra-modal imaging of *ex vivo* human mammary tissue (control) and easily differentiated the 2PAF-visible elastin fibers from SHG-visible collagen fibers in the extracellular matrix (Fig. 1(e), left two panels). We then carried out the same reprogramming of excitation and selectively imaged these elastin fibers through the SHG detection channel of the tetra-modal imaging (Fig. 1(e), right panel). Thus, endogenous elastin fibers can be revealed by 2PAF imaging using the excitation/detection wavelengths of (720/440 nm) [9], (880/515 nm) [18], (940/562 nm) [3],

and (1110/>570 nm) (this study), suggesting that elastin fiber monomers may be biologically assembled [19] into a form of J-aggregates to enable widely redshifted excitation and detection. The yellow (2PAF) optical marker of the tetra-modal imaging “labels” not only cellular FAD, but also extracellular elastin fibers. Similar versatility is also applicable to the cyan (3PAF) and magenta (THG) optical markers of the tetra-modal imaging (Fig. 1(a), lower panel), as described below.

Identification of cells by their cytoplasmic optical signatures (rather than their nuclei as in H&E or SF-vH&E) is straightforward in the image of mouse kidney, but nontrivial in a tetra-modal image of human breast tissue where the cyan optical marker indicates the presence of oxidized lipid-associated fluorescent species [20,21] (arrows; Fig. 1(f), upper panel) while the magenta optical marker seems to reveal the cytoplasm (or mitochondria) of some cells (arrowheads; Fig. 1(f), upper panel). To confirm this speculation, we used acridine orange (a nuclear dye) for fresh tissue labeling [22,23], and obtained a similar tetra-modal image within minutes after the labeling. The largely green-colored nuclei appear inside the magenta-colored cytoplasm through the SHG detection channel of the tetra-modal imaging, as expected from the emission spectrum of acridine orange (arrowheads; Fig. 1(f), lower panels). Acridine orange was excited through three-photon absorption, not through one-photon absorption [23] or two-photon absorption [22], demonstrating the advantage of the tetra-modal imaging in three-photon fluorescent imaging. Significant signal increase observed in the 2PAF channel (Fig. 2) is attributed to the binding artifacts of acridine orange, which is known to emit green fluorescence when binding to double-stranded DNA and red fluorescence when binding to DNA strand breaks [24]. The artifacts of this stain (non-specific binding, unpredictable tissue distribution, unexpected/unknown disturbance of biological/physiological functions) lend further support to the conclusions in our current manuscript based on stain-free slide-free histopathology.

This labeling-induced artifact may not be detectable by previously demonstrated structural imaging [22,23], but can be easily detected by our tetra-modal histochemical imaging because of its unique sensitivity to functional molecular/metabolic changes in the cells and tissues. To avoid unexpected labeling artifacts, we focused on label-free imaging in subsequent cell phenotyping, and employed the acridine orange staining only to validate any ambiguous cell identification by the cytoplasmic optical signatures (Table 2).

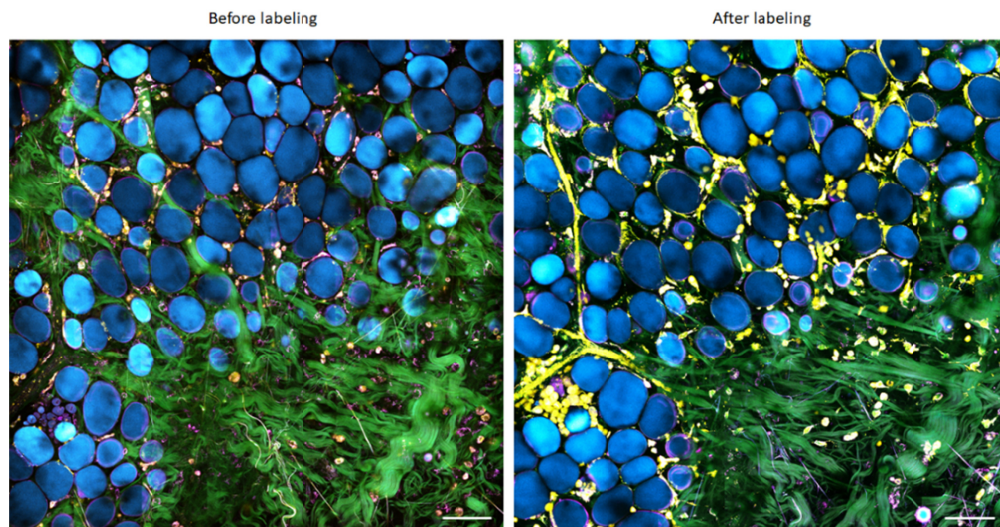


Fig. 2. Comparison of the tetra-modal images of normal mammary tissue before and after acridine orange labeling. Although labeling of nuclei is validated with green contrast (see Fig. 1(f)), many cells exhibit increased production of FAD (yellow contrast) associated with the labeling. Scale bars: 100  $\mu\text{m}$ .

**Table 2. Classified vital stromal or tumor cells in mammary tissue with distinct optical phenotypes.**

Cell type	Yellow cytoplasm	Yellow nucleus	Cyan cytoplasm	Cyan nucleus	Magenta cytoplasm	Magenta nucleus	Cell shape
<i>Rat and human normal cells</i>							
Fibroblast	1	0	0	0	0	0	spindle
Erythrocyte	1	0	0	0	0-1	0	round
immune cell 1	1	0	0	0	1	0	round-like
Yellow-colored stromal cell	1	0	0	0	0	0	amoeboid
<i>Rat and human cancer-associated cells</i>							
Tumor cells	0-1	0-1	0-1	0-1	0-1	0-1	diverse
Magenta-colored stromal cell	0	0	0	0	1	0	amoeboid
Cyan-colored stromal cell	0	0	1	0	0	0	amoeboid

Note: 1 – visible, 0 – not visible.

#### 4.2 Phenotyping vital cells from rat to human

We then conducted systematic *in vivo* tetra-modal imaging of various cells in rat mammary tissue under the same excitation conditions and at similar imaging depths (20-40  $\mu\text{m}$ ). The imaging revealed locations in the normal mammary tissue of a control rat, or in the tumor center, vicinity of the tumor boundary or margin, and in the peri-tumoral field of specimens from a pre-clinical carcinogen-injected mammary tumor rat model. All tetra-modal images were directly comparable after plotting the four pseudo-color contrasts of magenta, cyan, green, and yellow with the same set of dynamic ranges. A distinct cell phenotype was recognized by the visibility of yellow, cyan, and magenta optical markers from both the nucleus and cytoplasm, termed as the optical phenotype (Table 2). Comparison of histological images of the same sample has been provided as Fig. 2 in Part II of this study [10]. Combining the optical phenotype with the local context of the extracellular matrix, we recognized a wide variety of cells including stromal cells or fibroblasts, erythrocytes, immune cells, endothelial cells, and tumor cells within the authentic tumor microenvironment (Fig. 3). All these cells observed *in vivo* were also observed with the same optical phenotypes in fresh *ex vivo* mammary tissue <12 hrs after resection, allowing a time window for consistent and comparative imaging and analysis. The endothelial cells were recognized by their unique elongated shape as well as their context in which they were well-aligned along the direction of the vessel, which highly correlates with their typical histologic morphology. The different optical signatures could be attributed to their active metabolic status. Endothelial cells with cyan outlines indicated high NADH concentrations, which are associated with glycolysis as well as hypoxia. Endothelial cells with strong THG signals indicated the local presence of water around the cells [25].

Similar phenotypical heterogeneity is found in human breast tissue <12 hrs after resection (Figs. 3(o), 3(s)), with heterogeneous carcinogenesis similar to the animal model (Figs. 4, 5). Unique correspondences can be established between some rat and human cells according to their similar optical phenotypes and organization of their extracellular matrices (bidirectional arrows; Fig. 3). The magenta-yellow-colored rat immune cells with a round-like shape (arrowhead; Fig. 3(a)) have been validated by their wide presence in lymph nodes, and may be correlated with similar human cells in *ex vivo* tissue (arrowhead; Fig. 3(p)) that could be difficult to image *in vivo*. As expected, in both rat and human specimens, abundant yellow-colored normal stromal cells (Figs. 3(f), 3(k)) are widely present in the stromal regions of control and cancer-associated specimens (e.g., see [Visualization 1](#) corresponding to Fig. 3(b)). However, the unique presence of cyan- or magenta-colored cancer-associated cells in the latter distinguishes a tumorous stroma (Figs. 3(h), 3(m)) from a normal stroma (Figs. 3(f), 3(k)). Our cell phenotyping cannot only differentiate normal and cancer-associated stroma and mammary ducts, but also normal (or angiogenic) and cancer-associated blood vessels. In

normal blood vessels, cyan-colored endothelial cells form the vessel wall (arrowheads; Figs. 3(b), 3(q)) with plausible internal flow of yellow-colored erythrocytes (see [Visualization 3](#) corresponding to Fig. 3(g)), and can be easily differentiated from certain yellow-colored vessels/ducts (arrowheads; Figs. 3(c), 3(r)).

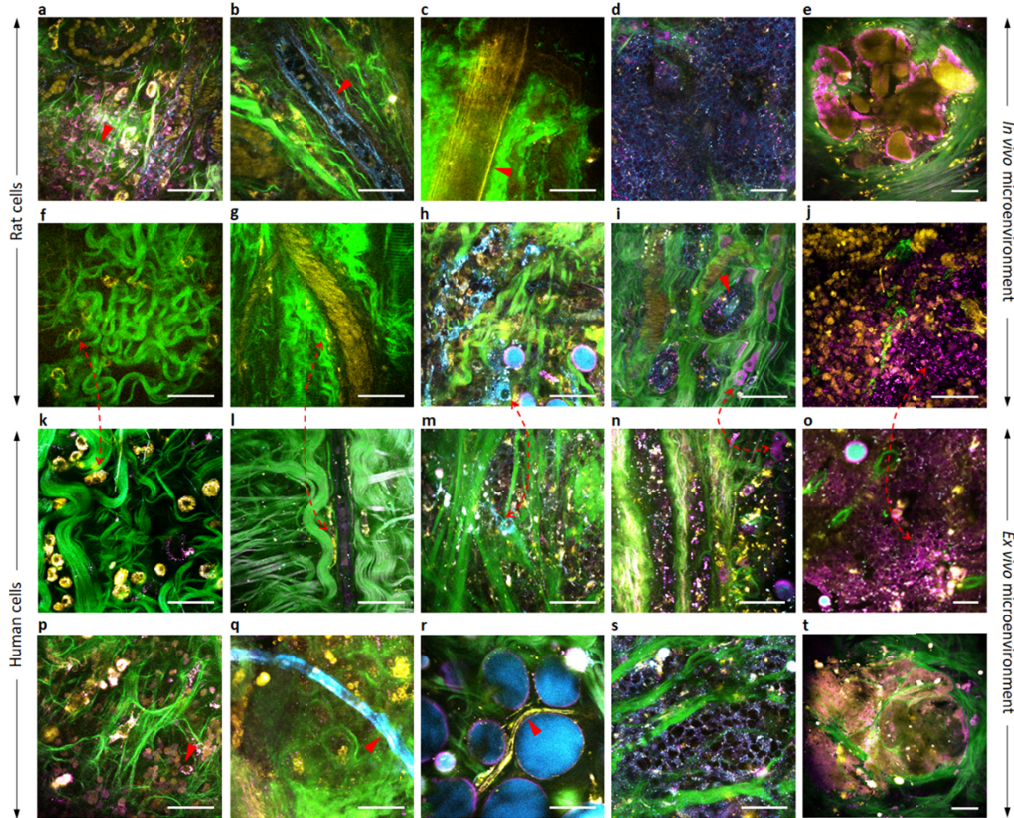


Fig. 3. Optical phenotyping of related rat mammary and human breast cells in different microenvironments by slide-free virtual histochemistry. (a) Rat immune cells in stroma. (b) Rat endothelial cells in a developing blood vessel ([Visualization 1](#)). (c) Rat tubular structure ([Visualization 2](#)). (d) Rat tumor cells with a largely cyan-colored cytoplasm. (e) Rat tumor structure. (f) Normal rat stromal cells. (g) Rat fibroblasts aligned with a blood vessel ([Visualization 3](#)). (h) Cyan-colored rat cancer-associated cells. (i) Magenta-colored rat cancer-associated cells (arrow) near mammary ducts (arrowhead). (j) Rat tumor cells with a magenta-colored cell body. (k) Normal human stromal cells. (l) Human fibroblasts aligned with a blood vessel. (m) Cyan-colored human cancer-associated cells. (n) Magenta-colored human cancer-associated cells (arrow) near mammary ducts. (o) Human tumor cells with a magenta-colored cytoplasm. (p) Human immune cells in stroma. (q) A plausible developing human blood vessel. (r) Human tubular structure. (s) Human tumor cells with a largely cyan-colored cytoplasm. (t) Human tumor structure ([Visualization 4](#)). Scale bars: 50  $\mu\text{m}$ .

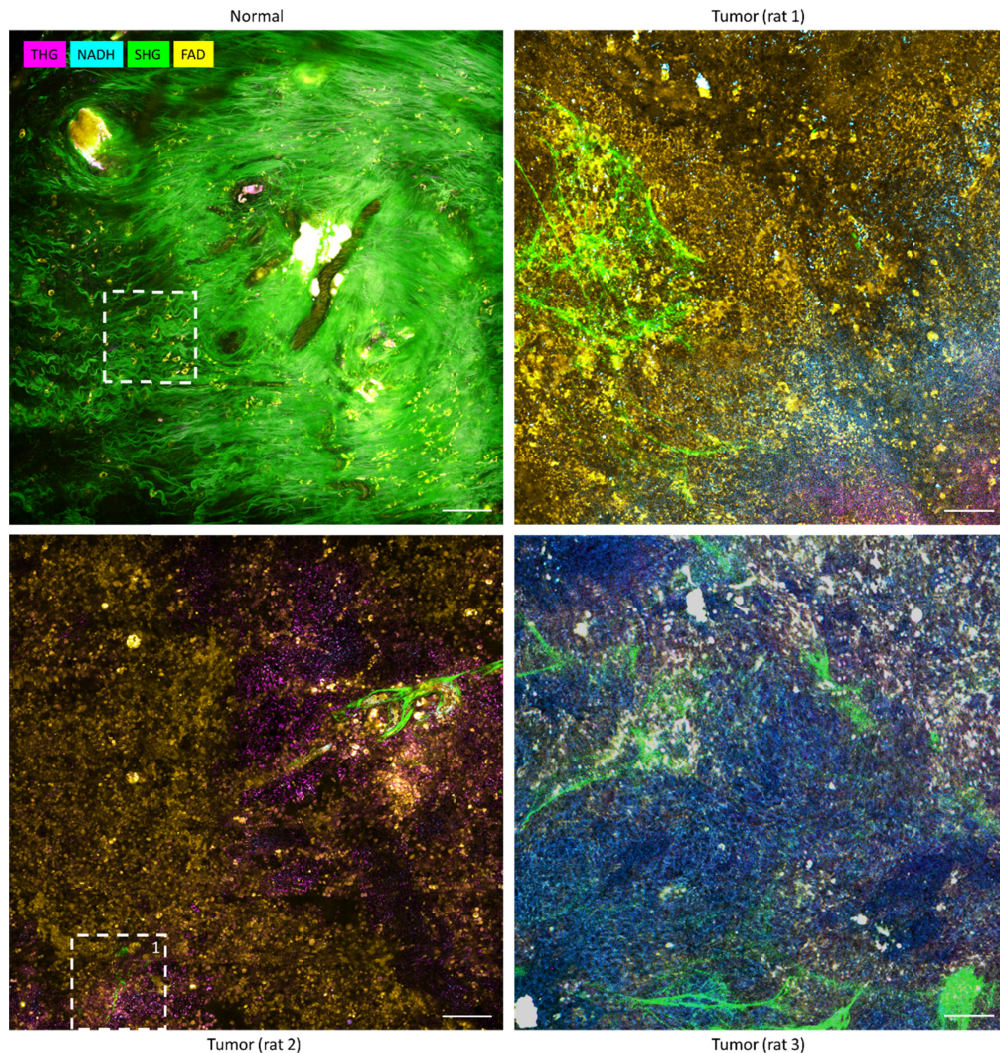


Fig. 4. Tetra-modal images of normal mammary tissue and tumors from different rats. Tumors from three different rats exhibit large heterogeneity in optical phenotype. Dashed box 1 is also plotted in Fig. 3(j). Scale bars: 100  $\mu\text{m}$ .

Our systematic tetra-modal imaging involves  $>10^5$  standard imaging fields-of-view ( $350 \times 350 \mu\text{m}^2$ , dictated by a high NA microscope objective) and hundreds of specimens from a moderately large number of rats ( $n = 26$ ) and human subjects ( $n = 20$ ), and produces a representative set of rat and human cells classified based on their optical phenotypes (Table 2). The histochemical specificity of our tetra-modal imaging is clearly demonstrated by phenotyping yellow-colored normal stromal cells and magenta- or cyan-colored cancer-associated cells in the stroma, which may be difficult to differentiate by standard (H&E) histology due to their similar amoeboid-like morphologies. As another example, elongated yellow-colored collagen-producing fibroblasts near blood vessels (bidirectional arrow; Figs. 3(g), 3(l)) can be easily differentiated by the tetra-modal imaging from elongated cyan-colored endothelial cells (arrowhead; Fig. 3(b)), but may be incorrectly interpreted as endothelial cells by standard histology due to their similarly elongated structures.

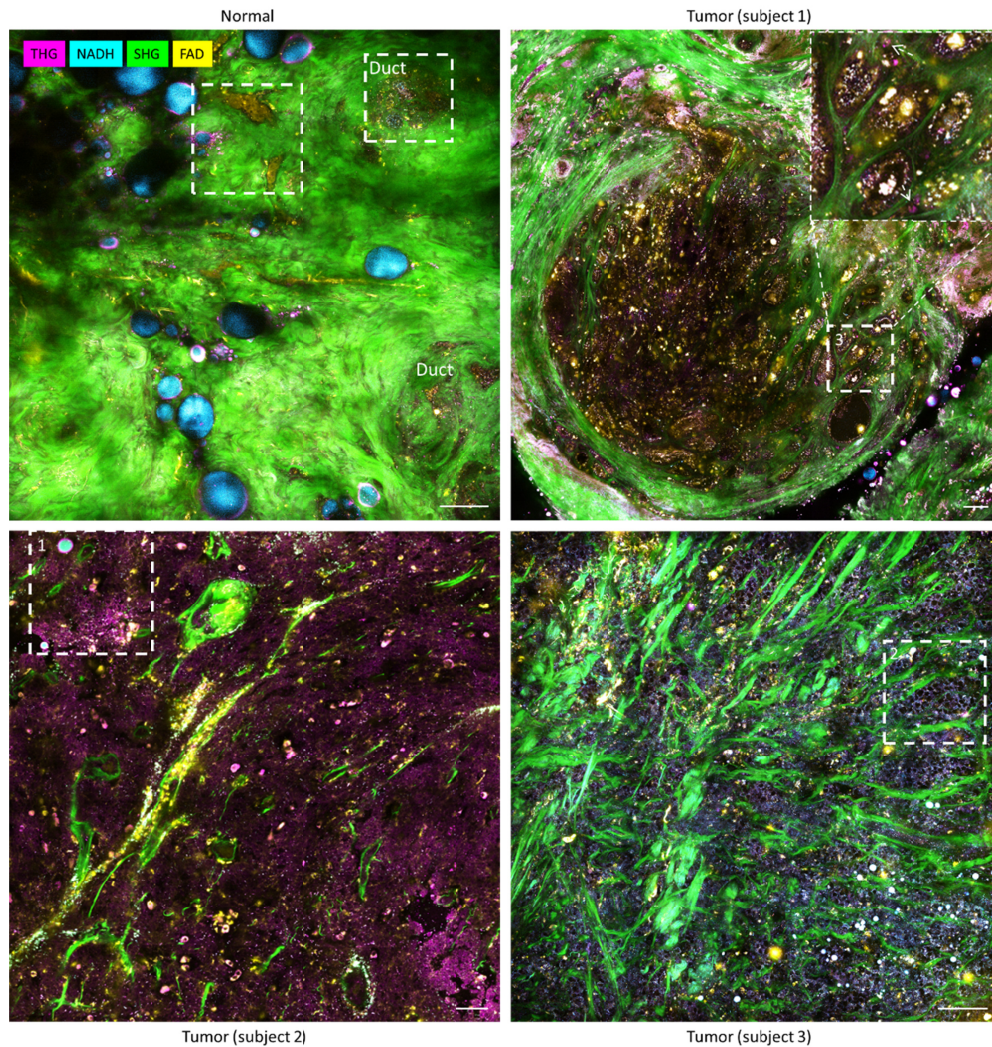


Fig. 5. Tetra-modal images of normal breast tissue and tumors from different human subjects. Tumors from three different patients exhibit large heterogeneity in optical phenotype. Dashed boxes 1 and 2 are also plotted in Figs. 3(o) and 3(s), respectively. Scale bars: 100  $\mu\text{m}$ . Dash box 3 shows magenta-colored stromal cells (arrows).

## 5. Discussion

In contrast to conventional histochemistry, the demonstrated slide-free virtual histochemistry shows great potential for fast general-purpose cell phenotyping because a relatively large number (four) of strictly co-localized histochemical contrasts can be imaged in a single tissue section *without interference*. This allows systematic in-tissue cell phenotyping for a given organ with straightforward translation of *in vivo* histochemical knowledge from animals to humans (Fig. 3 and Table 2), and simple adaption to non-breast organs such as kidney that exhibits rather different epithelial cells. Also, the ability of four largely bio-orthogonal optical markers to target both intracellular and extracellular biological substances (Fig. 1(a), lower panel) not only enables systematic in-tissue cell phenotyping but also classification of different stroma, epithelia, and vasculature, which would be difficult to achieve by four conventional histochemical markers. Moreover, the volumetric tetra-modal imaging clearly resolves three-dimensional ducts, blood vessels, and collagen structures with possibly

important biological implications ([Visualizations 1-4](#)), which are not routinely available from conventional histochemistry due to the additional time needed for serial sectioning and three-dimensional reconstruction of digitized slide images. It is to be noted that the 2PAF channel is not entirely specific to FAD, as multiple endogenous fluorophores (e.g. lipofuscin and porphyrin) share similar spectral characteristics in the spectral window of 600–650 nm [26]. It is by the combination of the 2PAF signal intensity and the cellular morphology, as well as the microenvironmental context, that we assigned the 2PAF channel largely to FAD, and subsequently analyzed the optical redox ratio for the identified cells. With the multimodal optical signatures collected with this system, there will likely be a continuum of values that represent a continuum of metabolic and molecular states. Along with the morphological features, these will combine to form the “optical phenotypes” we observe. Further investigations will be performed in the future to systematically establish the link between the optical phenotypes and different cell types. The focus areas of this paper are to demonstrate the clinical potential of our proposed imaging platform, to seek clues on the underlying carcinogenesis, and to reveal potential diagnostic markers.

Cahill et al developed another type of virtual H&E histology via high-speed multiphoton imaging, which demonstrated strong potential for margin assessment for breast cancer with the aid of stains [27]. In contrast, the system proposed in this work compromised imaging speed (pixel dwelling time 5–20  $\mu$ s) for label-free molecular profiling capability and highlights stain-free, slide-free, 3D, structural and functional imaging of cells and cellular dynamics in the authentic microenvironment. Although the relatively small fields-of-view make full tissue/margin assessment impractical, the high-dimensional molecular and functional changes revealed in the tumor micro- and macro-environments demonstrate the importance and the feasibility of characterizing the peri-tumor microenvironment for the underlying carcinogenesis as well as for potential diagnostic markers. The advantage of this system over existing label-free multimodal multiphoton microscopy systems is that it enables simultaneous and efficient excitation and detection of auto-fluorescence and harmonic generation from a vast array of cellular and stromal components in living tissue by using a single-excitation fiber-based source. We anticipate this technology and methodology will be an attractive complementary approach to existing clinical tissue assessment methods thanks to its label-free nature, technical simplicity, real-time functionality, versatility, and rich molecular/metabolic content [8].

Our demonstrated slide-free virtual histochemistry also complements the label-free histochemical imaging by SRS microscopy [1,4] or photoacoustic microscopy [2,5], which may achieve similar cell phenotyping by rapidly tuning the molecular vibration frequency or absorptive wavelength during the imaging. Our technique is based on well-established multiphoton microscopy with a long history of development. The compatibility of our technique with commercial multiphoton microscopy (Fig. 1(a)) may enable its more widespread use by simply replacing the standard Ti:sapphire laser in the microscope with our fiber laser-induced supercontinuum source. The latter is compact, reliable, and suitable for users without extensive laser training. The histochemical contrasts of the tetra-modal imaging (Fig. 1(a), lower panel) using 1110-nm single-band excitation can be expanded by reprogramming the fiber laser-induced supercontinuum to generate additional tailored histochemical contrasts [3]. Thus, we believe the demonstrated slide-free virtual histochemistry in this paper will provide an attractive way to conduct clinical histochemistry in comparison to various alternative techniques. As a prototypical demonstration, in the second part (Part II) of this two-part series study, we show how this slide-free virtual histochemistry is used to detect field cancerization in peri-tumoral fields [10].

## Funding

National Cancer Institute (R01CA166309 and R01CA213149); National Institute of Biomedical Imaging and Bioengineering (R01EB023232) of the National Institutes of Health.

## Acknowledgment

We thank Darold Spillman for his general technical support, Marina Marjanovic for securing human tissue specimens and obtaining relevant pathological reports, Art Camire and Tommi Hakulinen from Spectra-Physics for their support and the use of a 10 MHz Yb-based laser (femtoTrain), and Cecile Mukerjee and Yoann Zaouter at Amplitude Systemes for kindly supplying the fiber laser (Satsuma) to optimize the fiber supercontinuum source.

We thank Anna Higham, Kimberly Cradock, Natasha Luckey, and Z. George Liu from Carle Foundation Hospital for assisting in the acquisition and histological assessment of the human tissue specimens in this study. We also thank the Carle Research Office for assisting in the coordination and consenting in this human subjects research.

## Disclosures

S.A.B., H.T., and S.Y. are named inventors on patents filed by the University of Illinois at Urbana-Champaign related to the development of slide-free virtual histochemistry. All other authors declare that they have no competing financial interests.

S.A.B. and H.T. are co-founders and hold equity in LiveBx, LLC, which is commercializing laser source and imaging technology for slide-free stain-free histopathology.

## References

1. D. A. Orringer, B. Pandian, Y. S. Niknafs, T. C. Hollon, J. Boyle, S. Lewis, M. Garrard, S. L. Hervey-Jumper, H. J. L. Garton, C. O. Maher, J. A. Heth, O. Sagher, D. A. Wilkinson, M. Snuderl, S. Venneti, S. H. Ramkissoon, K. A. McFadden, A. Fisher-Hubbard, A. P. Lieberman, T. D. Johnson, X. S. Xie, J. K. Trautman, C. W. Freudiger, and S. Camelo-Piragua, "Rapid intraoperative histology of unprocessed surgical specimens via fibre-laser-based stimulated Raman scattering microscopy," *Nat. Biomed. Eng.* **1**(2), 0027 (2017).
2. T. T. W. Wong, R. Zhang, P. Hai, C. Zhang, M. A. Pleitez, R. L. Aft, D. V. Novack, and L. V. Wang, "Fast label-free multilayered histology-like imaging of human breast cancer by photoacoustic microscopy," *Sci. Adv.* **3**(5), e1602168 (2017).
3. H. Tu, Y. Liu, D. Turchinovich, M. Marjanovic, J. Lyngso, J. Lægsgaard, E. J. Chaney, Y. Zhao, S. You, W. L. Wilson, B. Xu, M. Dantus, and S. A. Boppart, "Stain-free histopathology by programmable supercontinuum pulses," *Nat. Photonics* **10**(8), 534–540 (2016).
4. R. He, Y. Xu, L. Zhang, S. Ma, X. Wang, D. Ye, and M. Ji, "Dual-phase stimulated Raman scattering microscopy for real-time two-color imaging," *Optica* **4**(1), 44–47 (2017).
5. B. Ning, M. J. Kennedy, A. J. Dixon, N. Sun, R. Cao, B. T. Soetikno, R. Chen, Q. Zhou, K. Kirk Shung, J. A. Hossack, and S. Hu, "Simultaneous photoacoustic microscopy of microvascular anatomy, oxygen saturation, and blood flow," *Opt. Lett.* **40**(6), 910–913 (2015).
6. S. W. Chu, I. H. Chen, T. M. Liu, P. C. Chen, C. K. Sun, and B. L. Lin, "Multimodal nonlinear spectral microscopy based on a femtosecond Cr:forsterite laser," *Opt. Lett.* **26**(23), 1909–1911 (2001).
7. S. Huang, A. A. Heikal, and W. W. Webb, "Two-photon fluorescence spectroscopy and microscopy of NAD(P)H and flavoprotein," *Biophys. J.* **82**(5), 2811–2825 (2002).
8. S. You, H. Tu, E. J. Chaney, Y. Sun, Y. Zhao, A. J. Bower, Y. Z. Liu, M. Marjanovic, S. Sinha, Y. Pu, and S. A. Boppart, "Intravital imaging by simultaneous label-free autofluorescence-multharmonic microscopy," *Nat. Commun.* **9**(1), 2125 (2018).
9. W. R. Zipfel, R. M. Williams, R. Christie, A. Y. Nikitin, B. T. Hyman, and W. W. Webb, "Live tissue intrinsic emission microscopy using multiphoton-excited native fluorescence and second harmonic generation," *Proc. Natl. Acad. Sci. U.S.A.* **100**(12), 7075–7080 (2003).
10. S. You, Y. Sun, E. J. Chaney, Y. Zhao, J. Chen, S. A. Boppart, and H. Tu, "Slide-free virtual histochemistry (Part II): Detection of field cancerization," *Biomed. Opt. Express* **9**, 5253–5268 (2018).
11. C. Xu and F. W. Wise, "Recent advances in fibre lasers for nonlinear microscopy," *Nat. Photonics* **7**(11), 875–882 (2013).
12. N. Nishizawa and J. Takayanagi, "Octave spanning high-quality supercontinuum generation in all-fiber system," *J. Opt. Soc. Am. B* **24**(8), 1786–1792 (2007).
13. L. E. Hooper, P. J. Mosley, A. C. Muir, W. J. Wadsworth, and J. C. Knight, "Coherent supercontinuum generation in photonic crystal fiber with all-normal group velocity dispersion," *Opt. Express* **19**(6), 4902–4907 (2011).
14. W. Liu, S. H. Chia, H. Y. Chung, R. Greinert, F. X. Kärtner, and G. Chang, "Energetic ultrafast fiber laser sources tunable in 1030-1215 nm for deep tissue multi-photon microscopy," *Opt. Express* **25**(6), 6822–6831 (2017).

15. H. Tu and S. A. Boppart, "Coherent fiber supercontinuum for biophotonics," *Laser Photonics Rev.* **7**(5), 628–645 (2013).
16. T. Sakimoto, M. I. Rosenblatt, and D. T. Azar, "Laser eye surgery for refractive errors," *Lancet* **367**(9520), 1432–1447 (2006).
17. T. Hato, S. Winfree, R. Day, R. M. Sandoval, B. A. Molitoris, M. C. Yoder, R. C. Wiggins, Y. Zheng, K. W. Dunn, and P. C. Dagher, "Two-photon intravital imaging fluorescence lifetime imaging of the kidney reveals cell-type specific metabolic signatures," *J. Am. Soc. Nephrol.* **28**(8), 2420–2430 (2017).
18. P. Friedl, K. Wolf, U. H. von Andrian, and G. Harms, "Biological second and third harmonic generation microscopy," *Curr. Protoc. Cell Biol.* Chapter 4, Unit 4.15 (2007).
19. J. E. Wagenseil and R. P. Mecham, "New insights into elastic fiber assembly," *Birth Defects Res. C Embryo Today* **81**(4), 229–240 (2007).
20. R. Datta, A. Alfonso-García, R. Cinco, and E. Gratton, "Fluorescence lifetime imaging of endogenous biomarker of oxidative stress," *Sci. Rep.* **5**(1), 9848 (2015).
21. C. A. Alonzo, S. Karaliota, D. Pouli, Z. Liu, K. P. Karalis, and I. Georgakoudi, "Two-photon excited fluorescence of intrinsic fluorophores enables label-free assessment of adipose tissue function," *Sci. Rep.* **6**(1), 31012 (2016).
22. Y. K. Tao, D. Shen, Y. Sheikine, O. O. Ahsen, H. H. Wang, D. B. Schmolze, N. B. Johnson, J. S. Brooker, A. E. Cable, J. L. Connolly, and J. G. Fujimoto, "Assessment of breast pathologies using nonlinear microscopy," *Proc. Natl. Acad. Sci. U.S.A.* **111**(43), 15304–15309 (2014).
23. A. K. Glaser, N. P. Reder, Y. Chen, E. F. McCarty, C. Yin, L. Wei, Y. Wang, L. D. True, and J. T. C. Liu, "Light-sheet microscopy for slide-free non-destructive pathology of large clinical specimens," *Nat. Biomed. Eng.* **1**(7), 0084 (2017).
24. A. Yagci, W. Murk, J. Stronk, and G. Huszar, "Spermatozoa bound to solid state hyaluronic acid show chromatin structure with high DNA chain integrity: an acridine orange fluorescence study," *J. Androl.* **31**(6), 566–572 (2010).
25. F. Aptel, N. Olivier, A. Deniset-Besseau, J. M. Legeais, K. Plamann, M. C. Schanne-Klein, and E. Beaurepaire, "Multimodal nonlinear imaging of the human cornea," *Invest. Ophthalmol. Vis. Sci.* **51**(5), 2459–2465 (2010).
26. A. C. Croce and G. Bottiroli, "Autofluorescence spectroscopy and imaging: a tool for biomedical research and diagnosis," *European journal of histochemistry*, *EJH* **58**, 4 (2014).
27. L. C. Cahill, M. G. Giacomelli, T. Yoshitake, H. Vardeh, B. E. Faulkner-Jones, J. L. Connolly, C. K. Sun, and J. G. Fujimoto, "Rapid virtual hematoxylin and eosin histology of breast tissue specimens using a compact fluorescence nonlinear microscope," *Lab. Invest.* **98**(1), 150–160 (2018).